INTERNATIONAL JOURNAL FOR NUMERICAL METHODS IN FLUIDS, VOL. 17, 49–74 (1993)

SPECTRAL METHODS FOR THE VISCOELASTIC TIME-DEPENDENT FLOW EQUATIONS WITH APPLICATIONS TO TAYLOR–COUETTE FLOW

MARIOS AVGOUSTI†, BAICHEN LIU‡ AND ANTONY N. BERIS*

Department of Chemical Engineering, University of Delaware, Newark, Delaware 19716, U.S.A.

SUMMARY

The time evolution of finite amplitude axisymmetric perturbations (Taylor cells) to the purely azimuthal, viscoelastic, cylindrical Couette flow was numerically simulated. Two time integration numerical methods were developed, both based on a pseudospectral spatial approximation of the variables, efficiently implemented using fast Poisson solvers and optimal filtering routines. The first method, applicable for finite Re numbers, is based on a time-splitting integration with the divergence-free condition enforced through an influence matrix technique. The second one, is based on a semi-implicit time integration of the constitutive equation with both the continuity and the momentum equations enforced as constraints. Stability results for an upper convected Maxwell fluid were obtained for the supercritical bifurcations, either steady or time-periodic, developed after the onset of instabilities in the primary flow. At small elasticity values, $\varepsilon \equiv De/Re$, the time integration of finite amplitude disturbances confirms the stability of the single branch of steady Taylor cells. At intermediate ε values the rotating wave family of time-periodic solutions developed at the onset of instability is stable, whereas the standing wave is found to be unstable. At high ε values, and in particular for the limit of creeping flow ($\varepsilon = \infty$), the present study shows that the rotating wave family is unstable and the standing (radial) wave is stable, in agreement with previous finite-element investigations. It is thus shown that spectral techniques provide a robust and computationally efficient method for the simulation of complex, non-linear, time-dependent viscoelastic flows.

KEY WORDS Spectral collocation method Influence matrix Viscoelastic Taylor–Couette flow Hopf bifurcations Rotating and standing wave.

1. INTRODUCTION

In this paper we pursue a numerical study of the dynamics of finite-amplitude, axisymmetric disturbances in the viscoelastic flow between two independently rotating, infinitely long concentric cylinders. The full system of equations is solved as an initial boundary value problem using a pseudospectral spatial discretization. Most of the earlier analyses on the viscoelastic Taylor–Couette problem were restricted to infinitesimal perturbations (linear stability analysis[1]). Only our study and the one by Northey *et al.*[2] investigate the evolution of finite-value amplitude

* Author to whom correspondence should be addressed.
† Present address: Polymer Processing Institute and Department of Chemical Engineering, Stevens Institute of Technology, Hoboken, New Jersey 07030, U.S.A.
‡ Present address: Department of Chemical Engineering, University of California at Los Angeles, Los Angeles, California 90024, U.S.A.

0271–2091/93/130049–26$18.00
© 1993 by John Wiley & Sons, Ltd.
Received 27 January 1992
Revised 18 December 1992

disturbances to the axisymmetric, viscoelastic Taylor–Couette problem by resorting to the numerical solution of the relevant time-dependent equations. However, for the viscous (Newtonian) Taylor–Couette flow problem, several studies have been reported in the literature over the last 30 years (see references immediately below) in which the development and evolution of finite amplitude perturbations have been numerically investigated.

With the advent of computers in the mid-1960s, the numerical solution of the full time-dependent, non-linear, Taylor–Couette problem for a Newtonian viscous fluid became feasible. The first numerical method that investigators used was finite differences. Some early research was performed by Capriz *et al.*,[3] who used finite difference approximations in both the radial and the axial directions to solve the axisymmetric viscous flow. Although the discretizations used were not fine enough to converge to a satisfactory accuracy and their code encountered numerical instabilities, they were able to simulate supercritical phenomena. Another early work was that of Meyer,[4] who used an explicit time-dependent code to study the development and evolution of axisymmetric vortices. Later, he combined a Fourier expansion in the azimuthal direction with finite difference approximations in the radial and axial directions in order to simulate wavy vortices.[5] Alonso and Macagno[6] adopted an implicit time-dependent scheme for the study of the axisymmetric flow. de Roquefort and Grillaud[7] used upwind differencing for the approximation of the convective terms and an implicit time integration with fractional time steps to stabilize the finite difference method.

During the last decade, spectral and mixed spectral/finite difference methods have emerged as a viable alternative to finite differences for the simulation of the non-linear flow problems. Extending Meyer's early attempt,[5] Meyer-Spasche and Keller[8] used Fourier expansions in the axial direction, together with finite difference in the radial one to solve the steady-state, axisymmetric Navier–Stokes equations for the Taylor–Couette flow. Moser *et al.*[9] adopted spectral expansions in all three directions, to solve for both axisymmetric and wavy vortices. One problem associated with the time-integration of incompressible Navier–Stokes equations, as pointed out by several authors,[10–24] is that the time-derivatives for the velocity involve the pressure, improper evaluation of which leads to violation of the incompressibility constraint. Among others, two partially implicit approaches were suggested to overcome this problem: a fractional step method[10,11,17] and a time-splitting/influence matrix scheme.[14–16] The influence matrix approach (in this case called Green's function method) was also followed by Marcus[25,26] in the most comprehensive work in the numerical simulation of Newtonian Taylor–Couette flow.

The time-splitting name, used to describe the influence matrix scheme mentioned above, is not really very descriptive and might cause confusion. The integration is not split in time as in Runge–Kutta or in the fractional step method; rather, the variables are updated in several stages. In the first stage, the velocity is updated due to the inertia terms in the momentum equation using an explicit linear multistep method. The new pressure is calculated in the second stage by solving a Poisson equation so that the new velocity vector, obtained in the third stage, is divergence free. The final velocity is obtained by implicitly integrating the (linear) viscous terms of the momentum equation in the third and last stage.

The Dirichlet boundary conditions for the pressure evaluation at the second stage are obtained using an influence (capacitance) matrix technique obtained through the imposition of the divergence-free velocity constraint on the solid boundary. These boundary conditions guarantee the divergence-free character of the velocity field everywhere in the flow domain[14] and the compatibility of the discretized equations to the governing equations of the problem (momentum and continuity).[14] The linear equations described by the influence matrix represent non-local compatibility conditions for the boundary values of the pressure. Similar equations are recovered from the discretization of the integral equations which are alternatively proposed in order to

enforce compatibility of the pressure boundary conditions with the incompressibility constraint in non-fractional-step methods of integration of the momentum equations.[18,21]

Previous applications of the above-mentioned time-splitting/influence matrix method were limited to high *Re* number Newtonian flows where the time dependency of the flow is dominated by the (non-linear) convective terms in the momentum equations.[15,16,25,26] In the present work the time-splitting scheme is extended to apply for a generalized momentum equation where there is an additional contribution to the stress tensor due to the flow viscoelasticity. The time-evolution for this additional flow variable is also evaluated semi-implicitly. There are important applications involving high *Re* viscoelastic flows (such as drag reduction[27]) where the scheme outlined above is directly applicable. However, most applications of importance to industrial manufacturing processes (like extrusion) involve high *De* but very small *Re* flows,[28] typically less than 10^{-2}. Thus, for the latter applications, a new algorithm appropriate for the inertialess regime of the governing equations is developed in this paper. In it, the generalized momentum equations (i.e. involving a viscoelastic stress contribution) are considered in the limit of $Re=0$ as a spatial constraint to the stress evolution in time dictated by a separate constitutive equation. In this approach, the handling of the momentum equation with respect to the stress variables exactly parallels that of the continuity equation with respect to the velocity in the limit of zero compressibility.

Alternatively to the primitive variable (velocity–pressure) formulation of the time-splitting/influence matrix method, a streamfunction–vorticity representation can be used where the influence matrix equations impose compatibility conditions on the boundary values for the vorticity which originate from the no-slip conditions for the velocity.[21] The presence of non-local compatibility conditions in both formalisms, as well as the same number of Poisson (or Helmholtz) equations that are required to be solved for every time step, make the computational workloads corresponding to either approach comparable. For illustration purposes, as well as in keeping with the previous trends, we used a primary variable formalism in our non-zero *Re* applications and a streamfunction–vorticity formation in our inertialess simulations. However, it should be emphasized that in principle either formalism can be used in the construction of either non-zero or zero *Re* algorithms.

The zero *Re* algorithm, based on a streamfunction–vorticity formalism, results in the solution of an inhomogeneous biharmonic problem. Its numerical stability turned out to be comparable, and in fact superior, to that of the non-zero *Re* method. For identical spatial discretizations between simulations using the inertial and inertialess algorithms, a time-step 50 times larger could be used with the second as compared with the first method. For the same inertialess (creeping) flow regime, Northey *et al.*[2] have also developed, concurrently with this work, a fully implicit finite element formulation which has allowed them to calculate steady time-periodic viscoelastic flows corresponding to the standing wave pattern setting in after the onset of instability. However, although the implicit scheme of their work allows for a larger time step, it also requires a computationally very expensive solution of a large set of non-linear equations. For a discretization that is uniform in r and z ($N \times N$ points), the implicit scheme requires a per time-step workload which is proportional to N^4 (the discretization matrix corresponding to the finite-element method having a sparse structure) instead of a workload associated with our proposed method, proportional to N^3 (see also Sections 3.2 and 4.1).

The fact that in either of the above algorithms, selective terms in the governing equations are treated implicitly and the rest explicitly with respect to time leads to a time integration scheme which is as stable as it could have been without ever having to solve anything more than a Poisson or Helmholtz equation. Furthermore, the terms for which an explicit integration would have imposed the most severe restrictions to the size of the time step, such as the pressure and

viscous terms, are handled implicitly. The success of this spectral scheme is related to the above-mentioned features which, in conjunction with the use of fast Poisson–Helmholtz solvers, allow for a computationally efficient update of the flow variables without imposing excessive stability restrictions on the time-step size. Using this technique, Marcus[25,26] was able to calculate several stable axisymmetric Taylor-vortex equilibria and non-axisymmetric wavy-vortex flows corresponding to one travelling wave for a Newtonian viscous fluid. One of the objectives of this work is to extend the numerical simulations into the viscoelastic, time-dependent regime, based on the idea of time-splitting integration and pseudospectral, spatial approximations under both inertial and inertialess conditions. Very recently, a similar approach was followed by Phillips and Soliman[29] in the solution of the inertial viscoelastic driven-cavity flow.

In a previous work,[30] we reported the linear stability analysis and the calculation of the secondary family branches corresponding to the purely azimuthal viscoelastic flow between two independently rotating, infinitely long, concentric cylinders (Taylor–Couette flow). Usually, the information supplied from this approach is sufficient to determine the stability of the secondary flow setting in after the onset of instability, as is the case for example at high Re and low De when the resulting secondary flow is steady. Under these circumstances, bifurcation theory[31,32] maintains that the secondary family is stable if the bifurcation is supercritical (exchange of stabilities with the primary family). However, when a Hopf bifurcation occurs, as is the case at moderate and high elasticity numbers ($\varepsilon = De/Re \geqslant O(1)$), the presence of symmetry in the problem causes the bifurcation to be doubly degenerate. As a result, several solution families develop corresponding to two different patterns: the standing waves with an axial reflection symmetry and the rotating waves with a spatio-temporal symmetry. Despite the fact that the branches corresponding to both these patterns were found to be supercritical,[30] bifurcation theory[32] asserts that one and only one of these branches must be stable while the other must be unstable. Moreover, the theory cannot distinguish, simply from the bifurcation diagram, which one of the two patterns is the stable one. The stability analysis of the secondary time-periodic families is the primary goal of this work, in conjunction with the development of robust and computationally efficient numerical techniques for time-dependent viscoelastic flow calculations.

In Section 2, we present the governing equations and the steady-state purely azimuthal solution. In Section 3, we present the adaptation of the time-splitting, non-zero Re algorithm to the viscoelastic Taylor–Couette flow. We also present two filtering techniques which were successfully used in order to remove high frequency, numerically induced oscillations from the solution. In Section 4, the streamfunction–vorticity, zero Re algorithm and its implementation to the Taylor–Couette flow is developed. Subsequently, in Section 5, transient simulations for different parameter values are shown and the significance of these results is discussed in view of the analysis of the interaction of bifurcations with symmetry discussed elsewhere.[30] Finally, the concluding remarks follow in Section 6.

2. THE GOVERNING SYSTEM OF EQUATIONS

Consider two infinitely long, concentric cylinders of radii r_1 and r_2, $r_1 < r_2$, with fluid confined in the annulus between them. For convenience the cylindrical co-ordinate system (r-θ-z), with the z-axis chosen as the common axis of the two cylinders, is used. In general, we are interested in describing the axisymmetric, axially periodic flow which occurs at large enough rotation rates of either one or both inner and outer cylinders, corresponding to angular velocities Ω_1 and Ω_2, respectively. The flow problem is characterized by two geometric, one kinematic and two flow dimensionless parameters: the ratio of the radii, $\xi = r_1/r_2$; the dimensionless axial wavelength $L = 2\pi/\alpha d$, where d is the gap width, $d = (r_2 - r_1)$ and α is the wavenumber corresponding to the

assumed periodicity in the axial direction; the ratio of the angular velocities, $\mu=\Omega_2/\Omega_1$; the Reynolds number, *Re*,

$$Re=\frac{dr_1\Omega_1\rho}{\eta_p}, \tag{1}$$

where η_p is the polymer viscosity and ρ the fluid density, representing as usual the ratio of inertia to viscous forces; and the Deborah number, *De*,

$$De=\frac{\lambda_1 r_1\Omega_1}{d}, \tag{2}$$

indicating the importance of the fluid relaxation time, λ_1, to the flow process characteristic time, $d/(r_1\Omega_1)$. The fluid relaxation time is the single most important physical quantity characterizing viscoelastic flow behaviour. It roughly represents the time scale over which the viscoelastic fluid exhibits a (partial) memory of its previous deformation state. In general, viscoelastic effects become important (in the sense that the fluid has a tendency to re-establish its previous deformation state) when *De* is larger than, or of the order, 1. Alternatively, instead of either one of the *De* or *Re* numbers, their ratio, the elasticity number ε,

$$\varepsilon=\frac{De}{Re}=\frac{\eta_p\lambda_1}{\rho d^2}=\frac{\nu_p}{D_\lambda}, \tag{3}$$

can be used. For a given fluid, the magnitude of the elasticity number indicates the importance of elastic versus inertia effects. Alternatively, the elasticity number can be physically interpreted as a viscoelastic Prandtl number with ν_p and D_λ being an appropriate kinematic viscosity and relaxational diffusivity, respectively. The elasticity number has the advantage of being solely a property of the fluid and not of the flow.

The governing equations for the incompressible, viscoelastic flow corresponding to the Oldroyd-B fluid model are expressed in dimensionless form as follows. The continuity equation for an incompressible flow is expressed by the divergence-free condition

$$\nabla\cdot\mathbf{v}=0. \tag{4}$$

The momentum equation is written (in order to enhance the stability of the numerical implementation) in its rotational form

$$\frac{\partial\mathbf{v}}{\partial t}=\mathbf{v}\times\omega+\frac{1}{Re}\nabla\cdot\left[\mathbf{T}+\frac{\kappa}{1-\kappa}\nabla\mathbf{v}\right]-\nabla p, \tag{5}$$

where κ is the ratio between the solvent viscosity η_s and the total viscosity $\eta\equiv\eta_s+\eta_p$ in the Oldroyd-B constitutive equation

$$\kappa=\eta_s/(\eta_s+\eta_p), \tag{6}$$

ω is the vorticity vector defined by

$$\omega=\nabla\times\mathbf{v}, \tag{7}$$

p is the dynamic pressure

$$p=\Pi+1/2\nabla(\mathbf{v}\cdot\mathbf{v}), \tag{8}$$

where Π is the hydrodynamic pressure and $\mathbf{T}$ is the elastic part (the viscoelastic contribution) of the extra stress tensor. The remaining viscous contribution to the stress scales with the 'solvent' viscosity, which does not necessarily coincide with the viscosity of the solvent but rather

represents a measure for the instantaneous viscous response of the 'glassy' modes within the viscoelastic system. The Oldroyd-B constitutive equation is then written as

$$\frac{\partial \mathbf{T}}{\partial t} = -\mathbf{v}\cdot\nabla\mathbf{T} + \mathbf{T}\cdot\nabla\mathbf{v} + \nabla\mathbf{v}^{\mathrm{T}}\cdot\mathbf{T} - \frac{1}{\mathbf{De}}(\mathbf{T} - \nabla\mathbf{v} - \nabla\mathbf{v}^{\mathrm{T}}), \tag{9}$$

and

$$\boldsymbol{\sigma} = -\Pi\boldsymbol{\delta} + \mathbf{T} + \frac{\kappa}{1-\kappa}(\nabla\mathbf{v} + \nabla\mathbf{v}^{\mathrm{T}}), \tag{10}$$

is the total stress tensor.

In the above dimensionless equations, the gap width d is used as the scale for length, the linear velocity of the inner cylinder, $r_1\Omega_1$, as the scale for velocity, and the mass in unit volume, ρd^3, as the scale for mass.

Equations (4), (5) and (9) are considered together with the non-slip, non-penetration boundary conditions on the cylinder walls,

$$\mathbf{v} = \begin{cases} \mathbf{e}_\theta & \text{at } r = r_1 = \dfrac{\zeta}{1-\zeta}, \\ \dfrac{\mu}{\zeta}\mathbf{e}_\theta & \text{at } r = r_2 = \dfrac{1}{1-\zeta}, \end{cases} \tag{11}$$

and the periodic boundary condition in the axial direction,

$$\mathbf{v}(z) = \mathbf{v}\left(z + \frac{2\pi}{\alpha}\right), \qquad \mathbf{T}(z) = \mathbf{T}\left(z + \frac{2\pi}{\alpha}\right), \tag{12}$$

where α is the periodicity number, or wavenumber.

The time-dependent integrations presented here refer to variables perturbing the primary (base) solution. This solution corresponds to the purely azimuthal steady-state Couette flow and is available in closed-form analytical expressions.[30]

3. TIME-SPLITTING/INFLUENCE MATRIX NON-ZERO *Re* ALGORITHM

A pseudospectral method, combined with a time-splitting/influence matrix technique, is used for the numerical solution of the time-dependent equations corresponding to the Taylor–Couette flow problem for an Oldroyd-B viscoelastic fluid model, equation (9). The method developed here is a slight variant of the Green's function technique used by Marcus[25] and the influence matrix technique used by Phillips and Soliman.[29] For the time-dependent viscoelastic flow calculations, the formulation of the equations is developed in the primitive variables: velocity, pressure and stress. At each time step, the velocity field is updated quasi-implicitly, the pressure implicitly, and the extra stresses explicitly, by using a three-stage time-splitting algorithm.

3.1. Method formulation

In the first stage, the velocity in the momentum equations and the stress in the constitutive equations are advanced in time, accounting explicitly for the non-linear terms and the elastic extra stresses in the momentum equations, and for all the terms in the constitutive equations,

using a second-order multistep Adams–Bashforth method:

$$\mathbf{v}^{n+1/3}=\mathbf{v}^n+\Delta t\left[\frac{3}{2}\left(\mathbf{v}\times\boldsymbol{\omega}+\frac{1}{Re}\nabla\cdot\mathbf{T}-\frac{1}{Re}\nabla^2\mathbf{v}\right)^n-\frac{1}{2}\left(\mathbf{v}\times\boldsymbol{\omega}+\frac{1}{Re}\nabla\cdot\mathbf{T}-\frac{1}{Re}\nabla^2\mathbf{v}\right)^{n-1}\right], \tag{13}$$

$$\mathbf{T}^{n+1}=\mathbf{T}^n+\Delta t\left\{\frac{3}{2}\left[-\mathbf{v}\cdot\nabla\mathbf{T}+\mathbf{T}\cdot\nabla\mathbf{v}+\nabla\mathbf{v}^{\mathrm{T}}\cdot\mathbf{T}-\frac{1}{De}(\mathbf{T}-\nabla\mathbf{v}-\nabla\mathbf{v}^{\mathrm{T}})\right]^n\right.$$
$$\left.-\frac{1}{2}\left[-\mathbf{v}\cdot\nabla\mathbf{T}+\mathbf{T}\cdot\nabla\mathbf{v}+\nabla\mathbf{v}^{\mathrm{T}}\cdot\mathbf{T}-\frac{1}{De}(\mathbf{T}-\nabla\cdot\mathbf{v}-\nabla\mathbf{v}^{\mathrm{T}})\right]^{n-1}\right\}. \tag{14}$$

In the second stage, an initial pressure correction is implemented implicitly,

$$\mathbf{v}^{n+2/3}=\mathbf{v}^{n+1/3}-\Delta t\nabla\tilde{p}^{n+1}, \tag{15}$$

where $\tilde{p}^{n+1}$ is evaluated by solving a Poisson equation,

$$\nabla\cdot\mathbf{v}^{n+1/3}=\Delta t\nabla^2\tilde{p}^{n+1}, \tag{16}$$

subject to the homogeneous boundary conditions, $\tilde{p}^{n+1}=0$, on the walls. Equation (16) is solved by using a fast Poisson solver which is based on a direct tensor method applicable for discretized PDEs with no mixed derivatives in a regular geometry such as Taylor–Couette flow.[13,33,34]

In the third stage, a viscous correction is calculated implicitly by solving a Helmholtz equation,

$$\tilde{\mathbf{v}}^{n+1}=\mathbf{v}^{n+2/3}+\frac{\Delta t}{Re(1-\kappa)}(\nabla^2\tilde{\mathbf{v}}^{n+1}), \tag{17}$$

subject to non-slip and non-penetration at the wall boundary conditions. This implicit updating is accomplished efficiently by again using a fast solver which is based on the fast Poisson solver discussed before, after some modification.[35]

An immediate consequence of equations (15), (16) and (17) is that the divergence of the final velocity field satisfies a Helmholtz equation (compare with the equation derived according to the SPPE approach in the continuous time limit on p. 1137 of Gresho and Sani[20])

$$\nabla\cdot\tilde{\mathbf{v}}^{n+1}=\frac{\Delta t}{Re(1-\kappa)}\nabla^2(\nabla\cdot\tilde{\mathbf{v}}^{n+1}), \tag{18}$$

the term involving the divergence of $\mathbf{v}^{n+2/3}$ being identically zero because of equation (16). Therefore, due to the linearity of the Helmholtz equation, the final velocity will be divergence-free if and only if it is divergence-free on the boundaries.[20] In addition to guaranteeing the equivalence of the pressure Poisson equation to the incompressibility constraint,[14,20] the divergence-free condition on the solid boundaries has also been found previously[25] to be critical for the stability of the numerical method. To implement it, steps 2 and 3 need to be repeated with non-homogeneous boundary conditions for the pressure as follows* (see References 18, 21 and 25 for an alternative but equivalent approach, using Green's functions). At the end of the $n+1$ time step, the corrected pressure, p^{n+1}, and velocity, $\mathbf{v}^{n+1}$, are obtained as

$$p^{n+1}=\tilde{p}^{n+1}+\sum_{i=1}^{k-1} f_i\, p_i, \tag{19}$$

* The approach described here, which leads to a set of linear equations between the boundary values of the pressure at the solid boundaries, is exactly what is called the 'influence matrix'[14,29,36] or 'capacitance matrix'[15] technique.

$$\mathbf{v}^{n+1} = \tilde{\mathbf{v}}^{n+1} + \sum_{i=1}^{k-1} f_i \mathbf{v}_i, \tag{20}$$

where the coefficients f_i, $i = 1, 2, \ldots, k-1$, with k being the total number of nodes on the cylinder walls, are chosen so as to make $\mathbf{v}^{n+1}$ divergence free on the boundary node $\mathbf{x}_i$. The trial solutions for the pressure, p_i, are obtained from the solution of a Laplace equation

$$\nabla^2 p_i = 0, \tag{21}$$

subject to the boundary conditions

$$p_i(\mathbf{x}_j) = \delta_{ij}, \tag{22}$$

where $\mathbf{x}_j$, $j = 1, \ldots, k$, denote nodal points at the cylinder walls (solid boundaries), and δ_{ij} is the Kronecker delta. The corresponding velocities, $\mathbf{v}_i$, are then obtained from $\mathbf{v}_i^{n+2/3}$,

$$\mathbf{v}_i^{n+2/3} = -\Delta t \nabla p_i, \tag{23}$$

by solving a Helmholtz equation similar to (17),

$$\mathbf{v}_i^{n+1} = \mathbf{v}_i^{n+2/3} + \frac{\Delta t}{Re(1-\kappa)} \nabla^2 \mathbf{v}_i^{n+1}. \tag{24}$$

Note that only $k-1$ modes are involved in the expansions provided by equations (19) and (20) because of the singular character of the equations due to the incompressibility condition. Indeed, the pressure at the kth mode can be assigned an arbitrary value.

In fractional step techniques,[10,11,17] the enforcement of the divergence-free condition by a projection of the final velocity field through a scalar field q does not necessarily imply an optimum approximation of the pressure P by q.[37,38] This is because the projection implemented at the very end of the velocity update procedure implies the approximation of a modified non-homogeneous Poisson equation for the scalar field q (equation (9) in Temam[37]). Although this modification was not found to change the accuracy of either the velocity or the pressure approximation in low-order (first-order in time) numerical schemes, this is not the case when higher-order time approximations are used.[38] In addition, the velocity only approximately satisfies the no-slip conditions at the solid boundaries.[17,37,38] In contrast, the use of a time-splitting approach leads to the correct form of Poisson equation for the pressure: equation (16) with $\mathbf{v}^{n+1/3}$ substituted by equation (13). Moreover, the final velocity update $\mathbf{v}^{n+1}$ obtained with the time-splitting/influence matrix technique described above satisfies exactly both the non-penetration and no-slip boundary conditions at the solid boundaries.

3.2. Method implementation

We now comment on the implementation of the numerical procedure and the accuracy and stability of the code. A spectral collocation (pseudospectral) method is used. The expansion functions used in the spectral representations are Chebyshev polynomials in the radial direction and Fourier sine and cosine trigonometric functions in the axial (periodic) direction involving M and N collocation points, respectively. The boundary conditions at the two rigid walls are that the velocity of the fluid must equal the velocity of the rotating wall.

Once the derivatives are spectrally evaluated, the updating of the variables due to the explicit part of the time-splitting procedure, (13) and (14), can be performed in a straightforward and inexpensive way. The most computationally demanding steps are the implicit updates in steps

2 and 3, requiring the solution of two Poisson and five scalar Helmholtz equations.† It is therefore imperative that fast solution techniques are used, since a typical run involves thousands of discrete time-step updates. For both Poisson and Helmholtz equations, the same approach of direct solution through tensor decomposition is used.[33,34,39] When either equation is spectrally discretized, a system of $(N \times M)$ linear algebraic equations is generated. Owing to the absence of mixed derivatives in the PDEs, the corresponding $(N \times M)$ by $(N \times M)$ square matrix can be written as the tensor product of two $(N \times N)$ and $(M \times M)$ square matrices. We exploit this fact by using a tensor product method to invert the matrix, as described by Lynch *et al.*,[33] Haidvogel and Zang[34] and Patera and Orszag.[39] In this way, for every right-hand side we reduce the number of operations to $O(N \times M^2, N^2 \times M)$ and the overall storage requirements[40] to $O(N \times M)$.

3.3. *Filtering*

The stability of the numerical procedure is governed by two factors. The first one is the Courant criterion, $\Delta t/\Delta x < 1$, which refers to the non-linear, convective-type terms appearing in the explicit steps (13) and (14). Owing to the use of Chebyshev spectral approximations which correspond to a non-uniform mesh concentrated towards the wall, the time step is forced to be $O(1/M^2)$. The second factor is the accumulation of the temporal discretization errors, introduced by step 1 and step 3, which are of the order $O[\Delta t, \Delta t/(Re(1-\kappa))]$, respectively. This accumulation of errors, coupled with the presence of numerically induced high frequency unstable eigenvectors,[30] results in the excitation of higher-order spectral modes, thus inducing high frequency oscillations in the solution. We used two equally effective ways to alleviate this problem.

The first approach is a filter suggested by Vichnevetsky and Bowles.[41] This is the exponential cutoff filter which for a two-dimensional Fourier fitted expression results in

$$g_{j,i}^{\text{filtered}} = g_{j,i}\rho_j\rho_i \qquad \text{(Fourier space)},$$

where

$$\rho_j = 1, \quad |j| < n_0 \tag{25}$$

$$\rho_j = \exp\left[-\beta\left(\frac{|j|-n_0}{n-n_0}\right)^4\right], \quad |j| \geqslant n_0,$$

$g_{i,j}$ is the variable in the Fourier space corresponding to the i, j mode in the two spatial directions and n is the total number of modes (equal in this case) in each direction. The point of cutoff is n_0 and β indicates how severely modes higher than n_0 are damped. A similar expression can be obtained for a Chebyshev approximated variable.

An alternative approach to filtering is the spectrum regularization technique. From previous applications of spectral methods to viscoelastic flows,[42] it has been seen that the magnitudes of the modes of the spectrum of a physical variable, such as velocity or stress, follow certain regular patterns with respect to the order of the mode, provided that the spatial variation of the variable is smooth enough. The spectrum of modes of such a smooth function can be divided into three frequency regions: low, intermediate and high. The amplitude of the low frequency modes varies in an unpredictable fashion following the transient variation of the flow variables. This is the most important part of the spectrum which determines the accuracy of the numerical approximation to

† The workload can actually be reduced to one Poisson and three scalar Helmholtz equations at the expense of increasing the storage requirements (by $4N^3$ words) through the precalculation and storage of the $4N$ Green's functions for the radial and axial velocity components corresponding to the $2N$ pressure modes.

the physical variable. The amplitude of the intermediate modes decreases with mode number, closely following a parabola or a straight line in a log–log plot of mode amplitude versus mode number. Finally, the amplitude of the high frequency modes usually varies in an irregular fashion because of numerical error. When numerical instabilities arise, they are usually manifested in an abnormal increase of the magnitude of the higher-order modes. This suggests the following rectifying procedure.

The original function, g, is first transformed into a series of Fourier or Chebyshev modes, $\hat{g}$. Then a simple relation between $\log|\hat{g}_i|$ and $\log(i)$, which can be linear or quadratic depending on the original function, is found through fitting of the $\log|\hat{g}_i| - \log(i)$ relationship of the intermediate modes (usually the middle third of the modes). The high frequency modes can then be 'regularized' by substituting their magnitude according to the fitting formula obtained from the previous relationship.

The parameters required by the spectrum regularization technique are the starting and the ending mode numbers for the intermediate mode region, n_0 and n_1, which can be found either from the analysis of the spectrum of the corresponding functions or from previous experience. In the calculations reported in this work, linear regression has been used to fit a straight line in a log–log plot of magnitude versus mode number with $n_0=(1/2)n$ and $n_1=(2/3)n$ for a total number of modes n. For further details on the implementation of the filtering techniques and the behaviour of the solution as the filtering parameters are changed, the interested reader is referred to the Ph.D. thesis by Liu.[35]

We used filtering on all the variables, mostly in the radial, and occasionally both in the radial and in the axial, directions (see also Section 5). The optimal frequency, the application of the filtering, was found to be once every 50 to 100 time steps. The effect of the filtering is discussed further below in Section 5.3 along with the analysis of the simulation results.

4. STREAMFUNCTION–VORTICITY ZERO *Re* ALGORITHM

4.1. Method development

In the limit of zero inertia, the momentum equation (5) reduces to

$$\nabla\cdot\left(\mathbf{T}+\frac{\kappa}{1-\kappa}\nabla\mathbf{v}\right)-\nabla p=0. \tag{26}$$

Note that the above relation does not contain any time derivatives and therefore it acts as an algebraic constraint to the discretized form of the governing equations. This realization led to the development of a new algorithm, which treats the momentum equations as constraints to the time evolution of the stress field as is dictated by the constitutive equations in a streamfunction–v_θ–vorticity formalism suitable for axisymmetric flows.

The divergence-free constraint is automatically satisfied for an axisymmetric flow by expressing the radial and axial components of the velocity, v_r and v_θ, in terms of the streamfunction, ϕ, as

$$\begin{aligned} v_r &= \frac{1}{r}\frac{\partial\phi}{\partial z}, \\ v_z &= -\frac{1}{r}\frac{\partial\phi}{\partial r}. \end{aligned} \tag{27}$$

The critical issue is then how to update the velocity field (the streamfunction ϕ, and the azimuthal velocity, v_θ). Following the standard approach for the solution of Stokes problems, the pressure is

eliminated by cross-differentiating and subtracting the r and z components of the momentum equation, (13), so that

$$\nabla \times \nabla \cdot \left(\mathbf{T} + \frac{\kappa}{1-\kappa} \nabla \mathbf{v} \right) = \nabla \times \nabla p = 0. \tag{28}$$

Equation (28) is a inhomogeneous, biharmonic equation with respect to the streamfunction. In the following, it is used as a constraint to any stress field update and is solved using a classical streamfunction–vorticity split with the Dirichlet boundary conditions for the vorticity obtained from the no-slip velocity conditions through an influence matrix approach.[21]

Moreover, the Oldroyd-B constitutive relation, equation (9), is written in the following form:

$$\frac{\mathrm{d}\mathbf{T}}{\mathrm{d}t} = \mathbf{f}(\mathbf{v}, \mathbf{T}) + \mathbf{g}(\mathbf{v}, \mathbf{T}), \tag{29}$$

where $\mathbf{f}$ represents the non-linear terms of the equation,

$$\mathbf{f}(\mathbf{v}, \mathbf{T}) = -\mathbf{v} \cdot \nabla \mathbf{T} + \mathbf{T} \cdot \nabla \mathbf{v} + \nabla \mathbf{v}^{\mathrm{T}} \cdot \mathbf{T}, \tag{30}$$

and $\mathbf{g}$ represents the linear terms,

$$\mathbf{g}(\mathbf{v}, \mathbf{T}) = \frac{1}{De} (\mathbf{T} - \nabla \mathbf{v} - \nabla \mathbf{v}^{\mathrm{T}}). \tag{31}$$

Equation (29) can now be formally integrated in time between two successive time steps, t_n and t_{n+1}:

$$\int_{t_n}^{t_{n+1}} \frac{\mathrm{d}\mathbf{T}}{\mathrm{d}t} \, \mathrm{d}t = \int_{t_n}^{t_{n+1}} \mathbf{f}(\mathbf{v}, \mathbf{T}) \, \mathrm{d}t + \int_{t_n}^{t_{n+1}} \mathbf{g}(\mathbf{v}, \mathbf{T}) \, \mathrm{d}t. \tag{32}$$

If the first integral on the right-hand side of (32) (non-linear terms) is evaluated using an Nth order explicit scheme and the second one (linear terms) using an Nth order implicit scheme, (32) is discretized in time as

$$\mathbf{T}^{n+1} = \mathbf{T}^n + \Delta t \sum_{i=1}^{N} \alpha_i \mathbf{f}^{n-N+i} + \Delta t \sum_{i=1}^{N+1} \beta_i \mathbf{g}^{n-N+i}. \tag{33}$$

More specifically, in the calculations reported in this work, an explicit second-order Moulton and an implicit second-order Adams–Bashforth method were used.

We now consider (28) at the $(n+1)$ time step and substitute for $\mathbf{T}^{n+1}$ from (33) while v_r and v_z are expressed in terms of ϕ using (27). By carrying out the algebraic manipulations, a non-homogeneous biharmonic problem in terms of the streamfunction, ϕ, is obtained,

$$E^4 \phi^{n+1} = h(\mathbf{T}^n, \ldots, \mathbf{T}^{n-N+1}, \phi^n, \ldots, \phi^{n-N+1}, v_\theta^n, \ldots, v_\theta^{n-N+1}, \Delta t, De, \kappa), \tag{34}$$

where the cylindrical operator, E, is defined by

$$E^2 = \nabla^2 - \frac{2}{r} \frac{\partial}{\partial r} = \frac{\partial}{\partial r^2} - \frac{1}{r} \frac{\partial}{\partial r} + \frac{\partial}{\partial z^2}. \tag{35}$$

Note that the right-hand side of (34) is expressed only in terms of known variables (i.e. corresponding to the time steps prior to $n+1$). This leads to the following solution algorithm. First, the updating of the streamfunction is obtained from the solution of (34). This equation is nothing more than a Stokes problem for ϕ^{n+1}, with a driving force on the right-hand side. The boundary conditions and the solution procedure of (34) are detailed in Section 4.1. Note that (34)

is an elliptic equation for ϕ^{n+1} which is close, in spirit, to the idea of the reformulation of the momentum equation to an explicitly elliptic form pioneered by King *et al.*[43]

Second, for the updating of v_θ, we insert (33) into the θ-component of (26) rather than (28) since, due to axisymmetry, the pressure does not appear in the θ-momentum equation. Therefore v_θ^{n+1} is obtained by solving a Poisson equation, with a right-hand side which contains only known quantities evaluated at the (n), ..., $(n-N+1)$ time steps. The boundary conditions are that the azimuthal velocity at the inner and outer rotating walls is constant and given as an input to the problem.

Finally, after obtaining the updated velocity field, $\mathbf{v}^{n+1}$, we employ (33) to get the stress field update, $\mathbf{T}^{n+1}$. The whole procedure, as described above, is then repeated at each time step. The temporal accuracy of the method is $O(\Delta t^N)$, and its stability is governed by the Courant criterion of the explicit part of (33), $\Delta t/\Delta x < 1$. The N value used in our calculations was 2.

4.1. The solution to the biharmonic problem

The key to the effectiveness of the proposed algorithm is in the efficient solution of the non-homogeneous, axisymmetric, biharmonic equation

$$E^4\phi = \text{RHS}, \tag{36}$$

where RHS is a known right-hand side function of r and z, which is independent of the dependent variables. The corresponding boundary conditions to (34) are the no-slip, non-penetration conditions at the wall, i.e.

$$v_r = v_z = 0, \quad \text{at} \quad r = r_1,\ r = r_2 \tag{37a}$$

expressed in terms of the streamfunction ϕ, (27) as

$$\phi = 0, \quad \frac{\partial \phi}{\partial r} = 0, \quad \text{on } \partial\Omega_{\text{solid}}. \tag{37b}$$

In order to apply the same direct tensor decomposition approach that we used for the solution of the Poisson and Helmholtz equations, (36) needs first to be decomposed into a set of separable PDEs. This can easily be achieved by considering a set of two equations

$$E^2\phi = w, \tag{38}$$

and

$$E^2 w = \text{RHS}, \tag{39}$$

where w is the vorticity, seen here as an auxiliary intermediate variable. Both equations (38) and (39) can now be solved efficiently by the direct tensor decomposition method exploiting the separable structure of the cylindrical operator E^2. In actuality, all these equations, i.e. the Poisson, Helmholtz and cylindrical operator problems, are numerically handled by the same subroutine which is only slightly modified as the particular type of equation changes.

The numerical procedure for the solution of the biharmonic equation involves three steps. In the first one, the inhomogeneous cylindrical equation

$$E^2 w^+ = \text{RHS}, \tag{40}$$

is solved subject to the homogeneous Dirichlet boundary conditions

$$w^+ = 0 \quad \text{on } \partial\Omega_{\text{solid}}, \tag{41}$$

In the second step another inhomogeneous cylindrical equation is solved

$$E^2\phi^+ = w^+, \tag{42}$$

also subject to the homogeneous Dirichlet boundary conditions

$$\phi^+ = 0 \quad \text{on } \partial\Omega_{\text{solid}}. \tag{43}$$

However, this procedure leads to a solution ϕ^+ which, in general, fails to satisfy the Neumann boundary condition,

$$\frac{\partial\phi}{\partial r} = 0 \quad \text{on } \partial\Omega_{\text{solid}}. \tag{44}$$

Consequently, a correction needs to be implemented in the third step of the solution. The solution ϕ is expressed as

$$\phi = \phi^+ + \sum_{i=1}^{k} f_i\phi_i, \tag{45}$$

where, ϕ_i is a Green's function of the biharmonic equation, i.e. ϕ_i satisfies the homogeneous biharmonic equation with inhomogeneous boundary conditions

$$\begin{aligned} \nabla^2 w_i &= 0 \qquad \text{with} \quad w_i(x_j) = \delta_{ij}, \\ \nabla^2\phi_i &= w_i \qquad \text{with} \quad \phi_i(x_i) = 0, \end{aligned} \tag{46}$$

and the coefficients f_i chosen such as to satisfy the von Neumann equation, (44), on the boundary. The coefficients f_i can thus be calculated by imposing (44) on the boundary nodes $i = 1, \ldots, k$ after substitution of (45),

$$\frac{\partial\phi}{\partial r}(x_j) = \frac{\partial\phi^+}{\partial r}(x_j) + \sum_{i=1}^{k} f_i \frac{\partial\phi_i}{\partial r}(x_j) = 0. \tag{47}$$

This approach leads to a set of k linear equations (compare the integral compatibility equations (30) provided by Dennis and Quartapelle[21] using a Green's function approach)

$$\sum_{i=1}^{k} \left[\frac{\partial\phi_i}{\partial r}(x_j) \right] f_i = -\frac{\partial\phi^+}{\partial r}(x_j). \tag{48}$$

Note that for the given problem, (48) is LU decomposed once in the beginning of the program so that for every time iteration only one pair of forward and back substitutions of total workload k^2 is necessary. Moreover, as was pointed out by a referee, the workload and storage requirements can be further reduced by taking into account that the boundary conditions corresponding to each axial wavelength are decoupled. Therefore, one has $k/2$ matrices each of which is 2×2 (since the values on the two cylinders remain coupled). Time and storage is now linear in k. This is also made clear by Marcus,[25] and it is one of the great advantages of a Fourier representation in a periodic direction. This decoupling also is present in the Poisson and Helmholtz problems.

The numerical implementation of the streamfunction–vorticity approach is basically similar to that of the time-splitting/influence matrix technique, where the LU decomposition of the matrix $[\nabla_r\phi_i(x_j)]$ and the solutions ϕ_is are constructed and stored only once in a pre-processing step. For the streamfunction–vorticity algorithm, the most computationally demanding step still remains the implicit evaluation of the biharmonic equations requiring the solution of one Poisson (for v_θ) and two biharmonic (for the streamfunction) equations, which are computationally

equivalent to five Poisson-type equations.‡ Thus, the streamfunction–vorticity formalism, if the evaluation of the pressure is not wanted, appears to be slightly more efficient, requiring both less computational work per time step and less storage. Indeed, it was used in implementing the non-zero *Re* algorithm with some computational gains. However, it is less general as it not applicable to fully 3D flows.

Both algorithms described in Sections 3 and 4 are very accurate (due to the involvement of spectral expansions) and very efficient in their implementation, both in terms of computational operations as well as storage. For an equal number N of Fourier and Chebyshev modes, the storage requirement increases linearly with the number of variables involved ($\propto N^2$), and the computational requirements only increase as the 3/2 power ($\propto (N^2)^{3/2}$), as opposed to a quadratic and cubic dependence, respectively, if a traditional Gaussian elimination technique were to be employed. Note that the use of fast Fourier transforms would have made the operation count to be asymptotically, for large N, almost linear ($\propto N^2 \log N$) with respect to the total number of unknowns, which is the absolute theoretical minimum. However, for the relatively small N used in this work ($N \leq 32$), there are no computational savings due to the higher value of the proportionality coefficients.[36]

5. RESULTS

Our investigation was focused on three regions, corresponding to small, medium and large values of the elasticity ratio ε. For comparison purposes, we used the same geometric parameters: the ratio of the inner to the outer radius, $\xi = 0{\cdot}95$, and the ratio of the inner to the outer rotational velocity, $\mu = 0{\cdot}5$. All the results which we show have been checked with mesh refinement, both in space and in time. The most refined spatial discretization used was $[16 \times 33]$, i.e. it involved 16 Fourier modes in the axial direction and 32 Chebyshev modes in the radial direction. The reported results were obtained, unless otherwise noted, using a mesh size $[16 \times 33]$. Note that the relatively small number of Fourier modes used was perfectly adequate for the purposes of this investigation, since the calculations are limited to the parameter region close to the bifurcation point where the incipient secondary flow involves just two Fourier modes (a cosine and a sine term).

The size of the time step varied depending on the value of the parameters and the type of algorithm used. For Newtonian fluids ($\varepsilon = 0$) and for calculations at small ε, $\varepsilon \ll 1$ (see Section 5.1), the dimensionless time step used was $\Delta t = 0{\cdot}1$. For intermediate values of ε, $\varepsilon = O(1) = 0{\cdot}24$ (see Section 5.2), the time step needed for a stable simulation was found to be $\Delta t = 0{\cdot}02$. For these particular calculations, filtering or regularization techniques were essential in order to obtain stable results, otherwise the required time step would have been prohibitively smaller. For the region of very large values of ε, $\varepsilon \gg 1$, i.e. $\varepsilon \sim 100$, the high *Re* time-splitting technique proved, as expected, to be very unstable. Therefore, in the limit of $Re = 0$, the creeping flow biharmonic algorithm described in Section 4 was used instead. Note that this limit is very well respected in traditional visco-elastic applications involving viscous materials. In these calculations, the time step restriction for stability was quite lax and stable simulations were obtained, without filtering, for $\Delta t = 1{\cdot}0$.

‡ Again, similarly to the time-splitting/influence matrix case (see footnote†), the workload can be reduced to one Poisson and one biharmonic equations at the expense of increasing the storage requirements (by $4N^3$ words) through the precalculation and storage of the $4N$ Green's functions for the streamfunction and the vorticity components corresponding to the $2N$ no-slip velocity modes.

For an initial perturbation to settle into a limit cycle, as we later show, the time integration had to be continued for many thousands of dimensionless units of time. As an example, for $\varepsilon = 0{\cdot}24$, with a grid size [16 × 33] (4752 unknown variables at each step) and $\Delta t = 0{\cdot}02$, a time integration for 1000 dimensionless units of time required about 1 CPU hour on the IBM 3090, or about 10 min on the Cray-Y/MP, running at about 15 MFLOPS on the IBM 3090 or 90 MFLOPS on the Cray-Y/MP. Even though the computational performance in MFLOPS of the creeping flow and high *Re* algorithms were comparable, in terms of actual time the simulation at $Re = 0$ was 50 times faster since the time step used there was 50 times larger, $\Delta t = 1{\cdot}0$. This allowed simulations very close to the bifurcation point to be performed where the dynamic changes are slow.

The main objective for the development of numerical algorithms and the use of the time-dependent simulations in this work was the investigation of the stability of the secondary flow branches developing supercritically under post critical conditions from the primary family of visco-elastic cylindrical Couette flow. Therefore, the following results first confirm and then complete (in terms of stability analysis) the findings of the linear stability analysis and bifurcation branch investigation presented previously.[30]

Both the high *Re* time-splitting and the inertialess biharmonic algorithm address initial boundary value problems. As such, it is necessary to initialize the calculations. One option, is to perform a 'cold start', i.e. start the simulation with the purely azimuthal Couette flow solution as the initial state and rely on computer 'noise' for the triggering of possible numerical instabilities which will act as mathematical imperfections. This approach is close to laboratory experimental conditions. However, it is a very expensive means of investigation because of the slow growth of the secondary flow near the critical bifurcation point. The other alternative is to use the eigenvector provided by the linear stability analysis to form a perturbation superimposed onto the Couette flow solution with an amplitude sufficient to speed up the realization of the final outcome. Another advantage of this approach is the capability at moderate and high ε of individually triggering the rotating or the standing wave instabilities through the use of the combination of eigenvectors corresponding to each pattern.

5.1. Validation procedure

An important component of our work was the capability to validate the transient solutions by comparing the results of the time integration algorithms to the predictions obtained from the independent linear stability analysis investigation, which in turn was also separately validated.[30] Table I depicts some representative results obtained from both the time-splitting method (non-zero *Re*) and the biharmonic (zero *Re*) algorithm. The eigenvalues shown in the last column of Table I are obtained from a non-linear regression of the time evolution of the radial velocity v_r, at a fixed point $\mathbf{x}_M$ in the domain. The comparison is extremely good, which proves that the transient behaviour of the system can be adequately reproduced, at least in the early stages of the instability development. It is also worth noting that, in accordance with the linear stability analysis investigation, runs with parameters which lie close to, but in the stable region of, the instability boundary showed a decrease and an eventual annihilation of any small initial perturbation. This performance is yet another indication of the faithful representation of the transient behaviour of the physical system by the numerical algorithms developed in this work.

5.2. Calculations at small ε

The simulations in this region of study were considerably simpler, faster and less expensive as compared to the rest of the computations since a relatively large time step was used, $\Delta t = 0{\cdot}1$, and

Table I. Validation of the initial value numerical codes

ε	Re	De	ζ	α	μ	σ	
						LSA*	IVP†
0·0	82·529	0·0	0·5	3·1	0·118	$1·539 \times 10^{-6}$	$1·529 \times 10^{-6}$
0·0	99·564	0·0	0·5	3·0	0·167	$8·246 \times 10^{-7}$	$8·339 \times 10^{-7}$
0·0	184·986	0·0	0·95	3·128	0·0	$2·657 \times 10^{-7}$	$2·687 \times 10^{-7}$
$5·7 \times 10^{-3}$	174·718	1·0	0·95	3·128	0·0	$-5·032 \times 10^{-7}$	$-5·024 \times 10^{-5}$
0·242	82·627	20·0	0·95	3·0	0·5	$-3·884 \times 10^{-7}$	$-3·959 \times 10^{-4}$
						$4·461 \times 10^{-2}$i	$4·484 \times 10^{-2}$i
∞	0·0	59·5	0·95	8·0	0·5	$5·145 \times 10^{-5}$	$5·210 \times 10^{-5}$
						$1·184 \times 10^{-2}$i	$1·184 \times 10^{-2}$i

* Results of linear stability analysis as a boundary value problem using 16 Chebyshev modes in the radial direction
† Results of the initial value numerical code using 16 Chebyshev modes in the radial direction and eight Fourier modes in the axial direction. The amplitude of the initial perturbation is $1·0 \times 10^{-7}$.

the resulting final state after the onset of the instability, that of a steady Taylor vortex flow, was established fairly quickly after the imposition of the initial perturbation.

Figure 1 shows the time evolution of a representative state variable, in this case the value of the radial velocity v_r at the particular location where it achieves its maximum amplitude in the computational domain, $\mathbf{x}_M$. This simulation was performed for the following parameters: $\varepsilon = 0·004$; $Re = 250$; $De = 1·0$; $\alpha = 3·0$; $\zeta = 0·95$; $\mu = 0·5$; $\kappa = 0·0$. Figure 2 shows the corresponding streamfunction contourlines for the established secondary flow at the new steady state. The equidistant contours depicted are normalized from $-1·0$ to $1·0$. The dashed lines indicate negative and the solid lines positive streamfunction values. The initial perturbation corresponds to the eigensolution obtained from the linearized equations. A direct comparison with the eigensolution (Figure 1 of Reference 30) shows that the final solution has no noticeable changes.

Note that these parametric conditions are situated well above the critical bifurcation point ($Re_c = 202·5$ for the same value of $De = 1·0$). The physically realizable solution in this case probably corresponds to a non-axisymmetric wavy Taylor vortex flow which cannot be captured by our investigation. However, the particular value of this example of viscoelastic flow simulations is to demonstrate that time-dependent calculations can be considered as an alternative way of calculating steady-state solutions. This is very important in viscoelastic flow simulations due to the large number of variables involved. The advantage over conventional steady-state finite element[43,44] or spectral/finite element[42] and pseudospectral/finite difference[45] calculations is in the savings in the storage and in the calculation of matrix inversions which, especially for three-dimensional applications, can be very substantial given that iterative techniques (for example, Picard iteration[44]) are not stable when applied to high De viscoelastic flow simulations.[44]

5.3. *Calculations at intermediate* ε

The time-dependent calculations in this region were performed starting from two different types of initial perturbation states, corresponding to the rotational and standing waves. These states were provided by the analysis of the bifurcation branches developed after the onset of instabilities.[30] The specific parameter space investigated is $\varepsilon = 0·2424$, $\zeta = 0·95$, $\mu = 0·5$ and $\kappa = 0·0$. From the neutral stability curve obtained by the linear stability analysis, the critical wavenumber was found to be $\alpha_c = 4·2$. The bifurcation point is located at $Re_c = 76·3$.

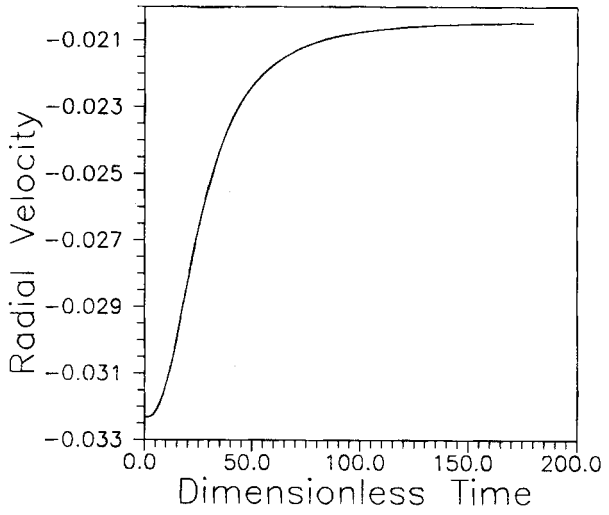

igure 1. Time evolution of v_r at $\mathbf{x}_M$ for the following parameters: $\varepsilon = 0{\cdot}004$; $Re = 250$; $De = 1$; $\alpha = 3{\cdot}0$; $\zeta = 0{\cdot}95$; $\mu = 0{\cdot}5$; $\kappa = 0{\cdot}0$

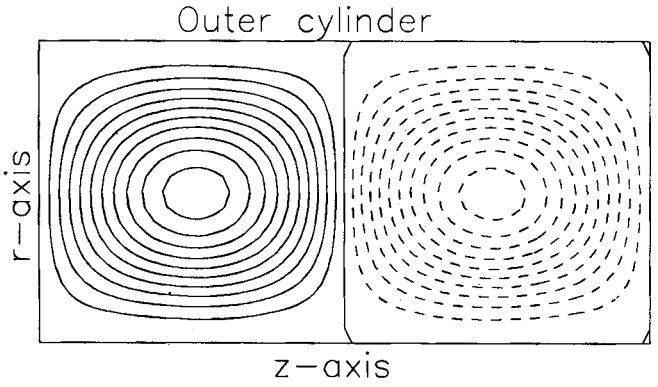

Figure 2. Normalized streamfunction contourlines for the established secondary flow at the new steady state for the parameters corresponding to Figure 1. The dashed lines correspond to depression and the solid lines to elevation regions

Figure 3 shows two simulations for the time evolution of v_r at a fixed location $\mathbf{x}_M$ (centre of the computational domain) for parameter values within the instability region, more specifically $Re = 76{\cdot}6$ (solid line) and $Re = 76{\cdot}7$ (dashed line), and for the initial condition of a rotating wave. From the two simulations, one can conclude that the secondary flow is oscillatory and settles into a stable limit cycle, evolving faster away from the bifurcation point. One can further conclude that the bifurcation is supercritical since the amplitude of the oscillation corresponding to the higher Re case is larger. This is in agreement with the bifurcation branch results already reported,[30] although the results are not directly comparable because of the use of a substantially coarser mesh in the non-linear investigations. Note that the small irregularities on the envelopes of the oscillatory curves shown in Figure 3 are due to coarse sampling and not due to any regular physical pattern or time integration errors. Figure 4 shows details from the last stages of the

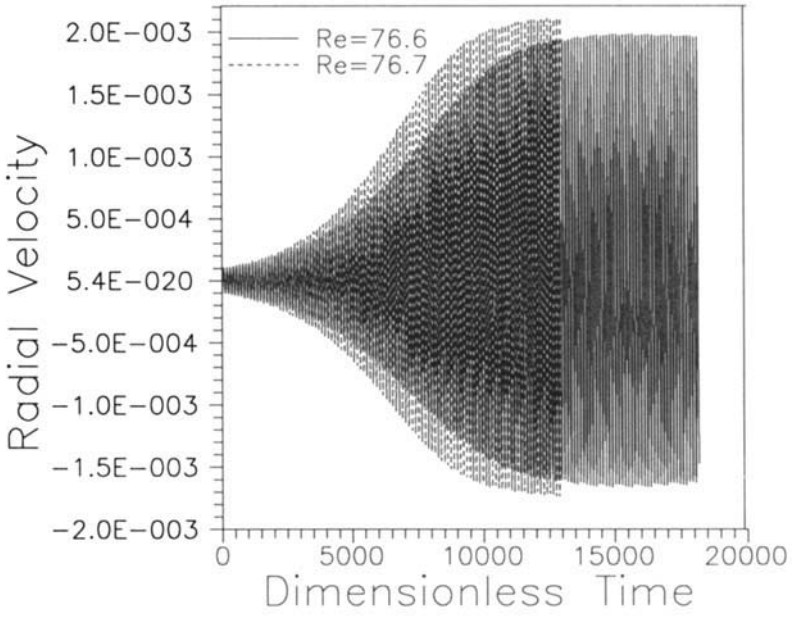

Figure 3. Time evolution of v_r at $\mathbf{x}_M$ for the following parameters: $\varepsilon=0{\cdot}24$; $De=18{\cdot}5$; $\alpha=4{\cdot}2$; $\zeta=0{\cdot}95$; $\mu=0{\cdot}5$; $\kappa=0{\cdot}0$ (rotating wave); $Re=76{\cdot}6$ (solid line); $Re=76{\cdot}7$ (dashed line)

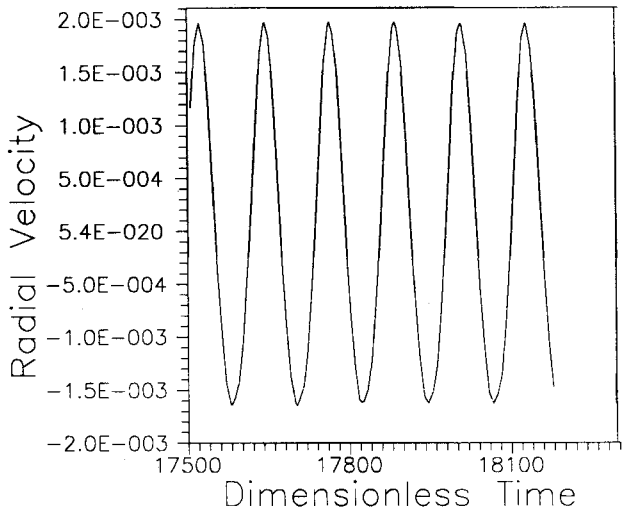

Figure 4. Magnification of the last stages of the simulation corresponding to the following parameters: $\varepsilon=0{\cdot}24$; $Re=76{\cdot}6$; $De=18{\cdot}5$; $\alpha=4{\cdot}2$; $\zeta=0{\cdot}95$; $\mu=0{\cdot}5$; $\kappa=0{\cdot}0$ (rotating wave)

simulation at $Re=76{\cdot}6$. It can be seen that the maximum amplitudes of the curve are not symmetric above and below the abscissa (time axis). Since the radial velocity is identically zero in the base (purely azimuthal) flow solution, this can be attributed to the effect of non-linearities of the problem and implies that higher harmonics are involved in the final limit-cycle solution.

Table II. Comparison between the linear stability analysis (LSA) and the simulation initial value problem (IVP) results for $\zeta=0{\cdot}95$, $\mu=0{\cdot}5$ and $\kappa=0{\cdot}0$

ε	Re	De	α	σ		Figure No.
				LSA	IVP	
0·2424	76·6	18·5	4·2	$0{\cdot}458\times10^{-3}$ $0{\cdot}513\times10^{-1}$i	$0{\cdot}431\times10^{-3}$ $0{\cdot}513\times10^{-1}$i	3
0·2424	76·7	18·5	4·2	$0{\cdot}515\times10^{-3}$ $0{\cdot}511\times10^{-1}$i	$0{\cdot}513\times10^{-3}$ $0{\cdot}511\times10^{-1}$i	3, 6
∞	0·0	59·5	8·0	$0{\cdot}510\times10^{-4}$ $0{\cdot}184\times10^{-1}$i	$0{\cdot}510\times10^{-4}$ $0{\cdot}184\times10^{-1}$i	9
∞	0·0	59·6	8·0	$0{\cdot}750\times10^{-4}$ $0{\cdot}184\times10^{-1}$i	$0{\cdot}750\times10^{-4}$ $0{\cdot}184\times10^{-1}$i	9
∞	0·0	60·0	8·0	$0{\cdot}170\times10^{-3}$ $0{\cdot}183\times10^{-1}$i	$0{\cdot}160\times10^{-3}$ $0{\cdot}183\times10^{-1}$i	8, 9

Through a non-linear regression applied to the early stages of the instability growth (up to 5000 dimensionless units of time), the oscillation frequency and its exponential amplification were found to agree very well with linear stability analysis results as indicated in Table II. The comparison was performed with the same number of Chebyshev modes. Figure 5 shows a snap-shot (corresponding to the parameters of Figure 3) of the streamfunction contourlines of the secondary stable oscillatory motion (limit cycle). As a direct comparison with the corresponding eigenvector (Figure 4 of Reference 30) shows, this solution is very close to the linear stability analysis prediction. A more careful comparison between the two solutions reveals a small increase in the inclination of the travelling wave. Note that due to the nature of the symmetries of this particular solution, no more snap-shots are necessary in order to visualize its evolution in time. The rotating wave simply translates in time along the z-axis, travelling one wavelength every period. Moreover, the direction corresponding to the positive translation of the travelling wave forms an obtuse angle with the separating streamline of the secondary Taylor flow cells. For example, the travelling wave represented in Figure 5, with Taylor cells inclined towards the outer cylinder, translates in the positive z-axis direction (left in Figure 5). Of course, due to the axial symmetry of the problem, there is another family of travelling waves corresponding to the mirror image (with respect to a horizontal plane) of those represented in Figure 5. These travelling waves, for which the secondary flow cells are inclined towards the inner cylinder, translate in the opposite direction (towards the negative z-axis).

According to the theory of bifurcation with symmetry (Section 4 of Reference 30), since the rotating wave pattern has been found to be stable, the other branch, that of the standing wave, should be unstable. Indeed, as Figure 6 shows, at $Re=76{\cdot}6$, a standing wave initial perturbation increases exponentially with time up to the point where the code (for the same fixed time step size) becomes numerically unstable. Repeated attempts with different initial amplitudes of the perturbation and at different Re have all failed to produce a stable limit cycle solution. In all these attempts the increasing amplitude of the secondary flow with time ultimately places the utilized time step size beyond that corresponding to the limit of stability (as defined by the Courant criterion), thus eventually causing the divergence of the numerical scheme. It is anticipated that the same limit cycle corresponding to a travelling wave would have been recovered if a small enough time-step size had been used. Unfortunately, the increased computational workload resulting from a small time step size and an anticipated long transient make these calculations

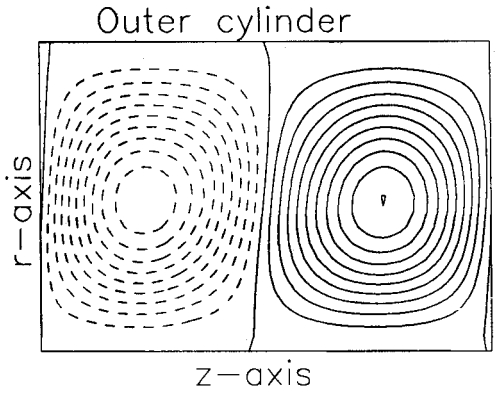

Figure 5. Snap-shot of the normalized and equidistant streamfunction contourlines for the established secondary flow at the new state for the parameters corresponding to Figure 3 and $Re = 76{\cdot}6$. The solution is a travelling wave

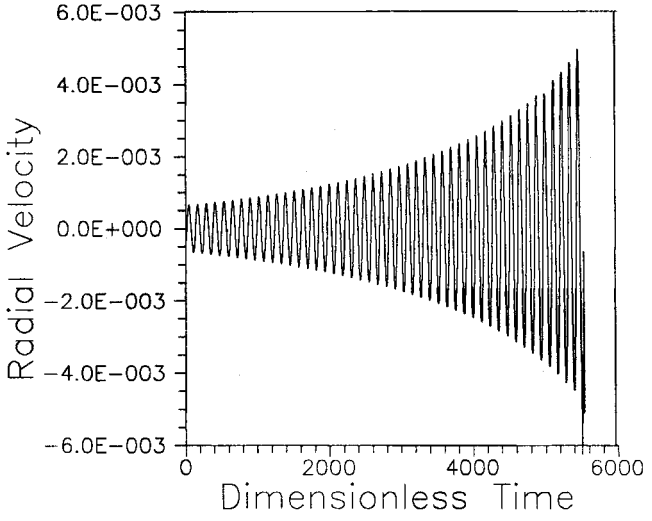

Figure 6. Time evolution of v_r at $\mathbf{x}_M$ for the following parameters: $\varepsilon = 0{\cdot}24$; $Re = 76{\cdot}7$; $De = 18{\cdot}5$; $\alpha = 4{\cdot}2$; $\zeta = 0{\cdot}95$; $\mu = 0{\cdot}5$; $\kappa = 0{\cdot}0$ (standing wave)

impractical with the available computational resources and, as a consequence, they were not carried out. Of course, as expected, for $Re < Re_c = 76{\cdot}3$ the initial perturbation, irrespective of the symmetry, was always found to decay to zero.

In all the previous calculations for small and moderate elasticity values, filtering techniques have proved to be a very effective tool for stabilizing the numerical integration. Essentially, (37) has been used with $\beta = 1{\cdot}0$ and $n_0 = 0{\cdot}5n$, where n is the total number of modes in the particular direction that the filter is employed. The filter is applied once every 50–100 time steps. Figure 7 shows the time evolution for the solution obtained with the parameters of Figure 6 with (dashed line) and without (solid line) filtering. One can readily appreciate the dramatic benefit

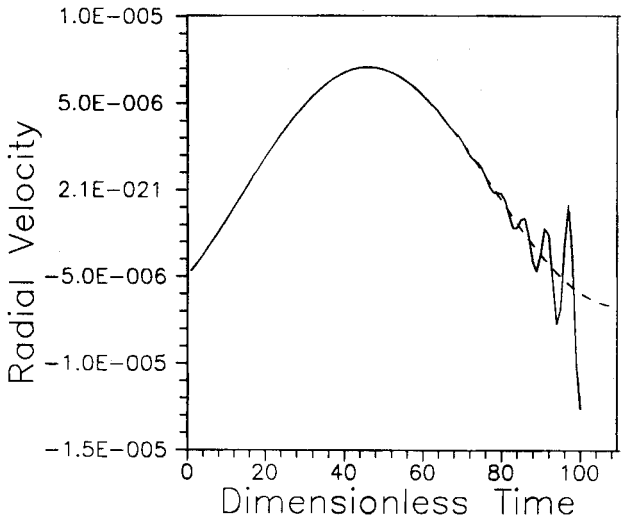

Figure 7. Time evolution of v_r at $\mathbf{x}_M$ for the following parameters: $\varepsilon = 0{\cdot}24$; $Re = 76{\cdot}7$; $De = 18{\cdot}5$; $\alpha = 4{\cdot}2$; $\zeta = 0{\cdot}95$; $\mu = 0{\cdot}5$; $\kappa = 0{\cdot}0$ (standing wave). The continuous line corresponds to the unfiltered solution and the dashed line to the filtered solution

brought about by the periodic use of filtering. We have also occasionally used the spectral regularization technique with similar success.

5.4. Calculations at infinite ε (creeping flow conditions)

All the simulations reported in this subsection were performed using the biharmonic algorithm described in Section 4, with constant time step $\Delta t = 1{\cdot}0$. They all correspond to zero inertia conditions ($Re = 0$). As with the results reported in the previous subsection, the two possible states which are used as initial conditions correspond to the rotating and standing wave patterns realized in the critical eigenvector space at the bifurcation point. The parameters used throughout are $\zeta = 0{\cdot}95$, $\mu = 0{\cdot}5$ and $\kappa = 0{\cdot}0$. The critical wavenumber which is evaluated from the linear stability analysis is $\alpha_c = 8{\cdot}0$. For these parameters, the onset of instability occurs at $De_c = 59{\cdot}4$.

The simulation of the rotating wave perturbation at post-critical conditions ($De = 60{\cdot}0$), as seen in Figure 8, grows exponentially up to a point where no matter how small the time step is set, the numerical solution diverged. This numerical instability, always observed when the amplitude of the secondary flow exceeds a certain level, seems to be related to the sensitivity of the Maxwell model to high frequency modes (as revealed from the flattening of the normal stability curves for high wavenumbers—see Reference 30) and limits the range at which any post-critical solution can be obtained (irrespective of the initial conditions) close to the bifurcation point. Simulations closer to the critical bifurcation point presented the same behaviour with much slower growth rates. This indicates that the rotating wave is not a stable solution to the problem. On the other hand, when a standing (radial) wave perturbation of small enough amplitude is used as an initial condition, then the post-critical simulation grows into a steady oscillatory motion, as shown in the composite plot of Figure 9 for $De = 59{\cdot}5$, $De = 59{\cdot}6$ and $De = 60{\cdot}0$. The magnitude of oscillation is increased as the De number increases and hence the bifurcation is supercritical. These results confirm the bifurcation diagrams calculated previously.

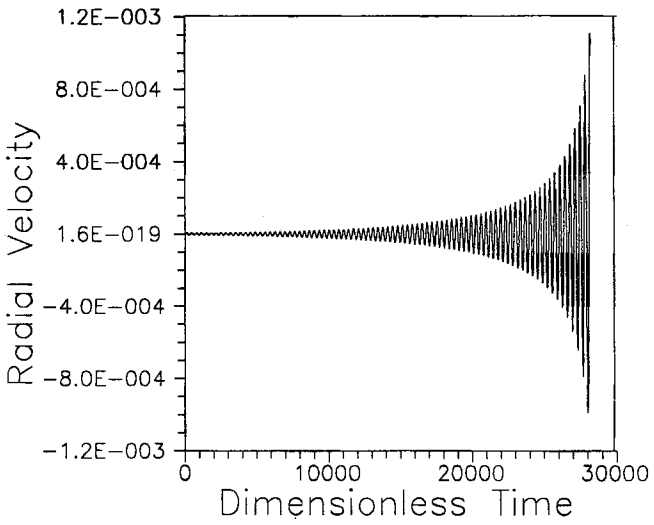

Figure 8. Time evolution of v_r at x_M for the following parameters: $\varepsilon = \infty$; $Re = 0$; $De = 60{\cdot}0$; $\alpha = 8{\cdot}0$; $\zeta = 0{\cdot}95$; $\mu = 0{\cdot}5$; $\kappa = 0{\cdot}0$ (rotating wave)

The growth rates and the oscillation frequencies exactly match those predicted by the linearized results shown in Table II. Again, an asymmetry is seen in the solution with respect to the location of the maxima and minima of the enveloped curves which indicates the presence of higher harmonics. From Figure 9 it is clear that as De is moved farther away from the critical point, De_c, the limit cycle solution becomes more asymmetric, as for example the simulation for $De = 60{\cdot}0$ indicates. The effect of non-linearities is also reflected in the streamfunction contour-lines shown in Figure 10. The four consecutive time snapshots correspond to the steady limit-cycle solution at $De = 60{\cdot}0$ of Figure 9. Each picture lies 1/8th of a period away from its neighbour. The solution satisfies the defining symmetries of the standing wave pattern (equation (4.4) of Reference 30). However, the skew-reflection symmetry $\phi(z, t) = -\phi(-z, t)$ present in the original eigenvector (obtained from the linear stability analysis), due to its sinusoidal time-dependence, is no longer satisfied. Therefore, simulation along the full wavelength is necessary. Furthermore, a comparison with the linear stability analysis results[30] shows a small but noticeable distortion of the radially travelling vortices which suggests that non-linear effects come into play.

In comparison to the moderate ε results, it is interesting to note here that as ε increases from 0·24 to ∞, the rotating and the standing wave branches exchange stabilities. As explained,[30] the standing wave family of solutions bifurcating at large values of ε ($\varepsilon \gtrsim 3{\cdot}4$ for the geometric and fluid parameters considered in this work) is a different family from that at intermediate values of ε (approximately ε between 0·12 and 3·4, see Figure 13 of Reference 30). The standing wave solution at $Re = 0$, shown in Figure 10, is also described as a radial wave and is shown here to be stable. In contrast, the standing wave solution for intermediate values of ε is unstable, whereas the rotating wave solution shown in Figure 5 is stable.

6. CONCLUSIONS

The primary objective of this work was to develop a robust computational method to enable the systematic investigation of complex time-dependent multidimensional non-Newtonian flows. The

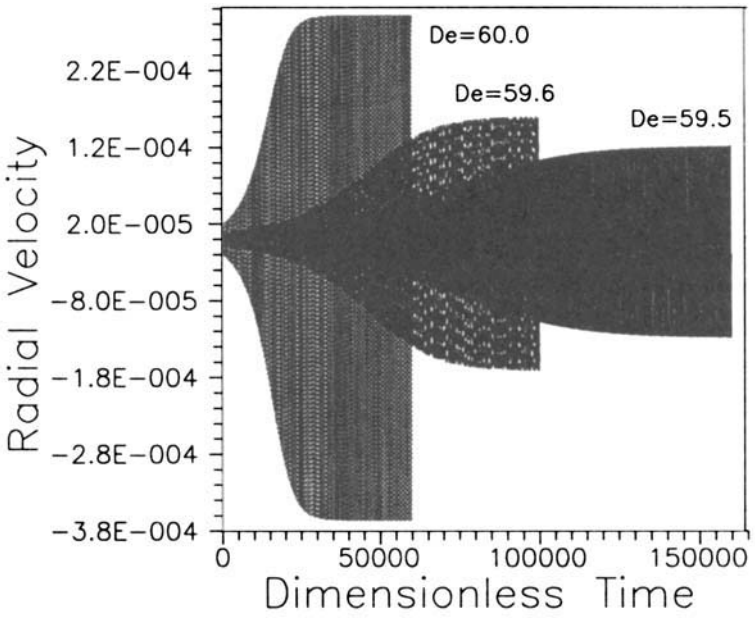

Figure 9. Time evolution of v_r at $\mathbf{x}_M$ for the following parameters: $\varepsilon = \infty$; $Re = 0{\cdot}0$; $\alpha = 8{\cdot}0$; $\zeta = 0{\cdot}95$; $\mu = 0{\cdot}5$; $\kappa = 0{\cdot}0$ (standing wave); $De = 59{\cdot}5$ (——); $De = 59{\cdot}6$; (— — —); $De = 60{\cdot}0$ (.....)

particular problem which was addressed was the non-linear evolution of viscoelastic Taylor–Couette instabilities. Two numerical techniques were developed, one applicable for high *Re* and the other for creeping flows, both of which rely on an efficient implementation of pseudospectral methods. The principles used are very general and apply to the investigation of numerous complex dynamical systems.

These spectral methods, efficiently implemented through the use of fast numerical solvers, proved to be particularly successful for the Taylor–Couette problem, where time-dependent simulations were sucessfully performed over hundreds of thousands of time steps for a broad range of the parameter values. The stability of the Taylor–Couette flow corresponding to three different modes, each one being the most unstable one in three distinctive regions in the *De–Re* parameter space, was investigated. In all cases, the bifurcations were found to be supercritical. For intermediate values of the elasticity number ε, the stable branch is that corresponding to a wave travelling in the z-direction, with symmetries described by those of a rotating wave. However, for large values of ε and in the limit of creeping flow, the stable solution branch changes form and its symmetries are now described by those of a standing wave. This solution corresponds to a radially travelling wave. This zero *Re* bifurcation picture is in agreement with the simulations performed by Northey *et al.*[2]

The numerical ability to simulate large non-linear systems dynamically may facilitate investigations for higher-order instabilities along the lines of the work of Kevrekidis *et al.*[46] The Taylor–Couette flow problem is particularly well suited for study because its solutions are fairly smooth and free of any discontinuities or large derivatives.[47] Caution should be exercised in using spectral methods where the expected solution possesses very steep gradients. In this case, one should probably use spectral elements, as suggested by Rønquist.[48] These methods also have the

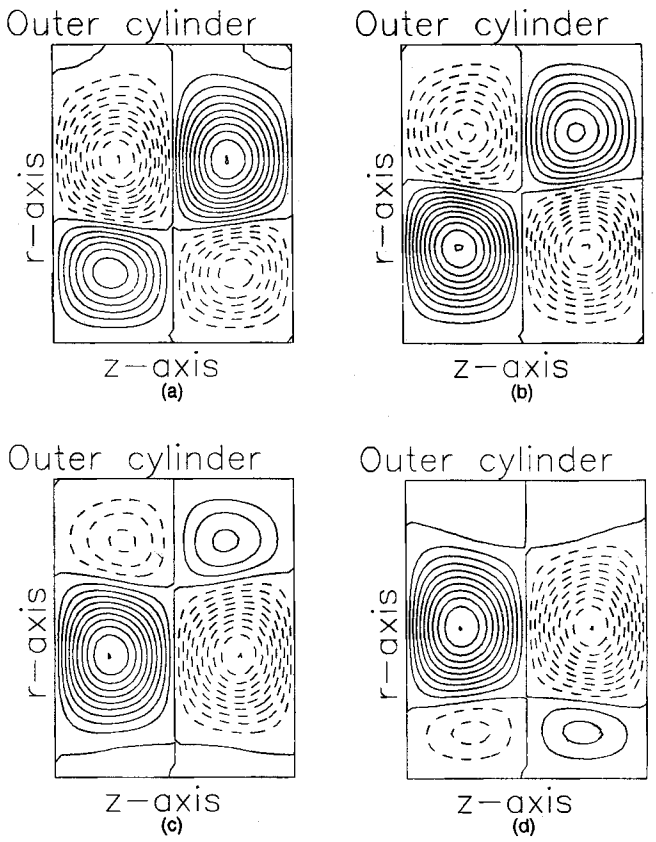

Figure 10. Dynamic behaviour of the established standing wave solution at four consecutive time snap-shots (Figures 10(a)–10(d)), showing the streamfunction contourlines, 1/8th of a period apart, corresponding to the parameters of Figure 9 for $De = 60{\cdot}0$. The maximum value of the streamfunction does not change in time

major advantage of being adaptable to flows within complex geometries. Clearly, more work needs to be done along these lines with viscoelastic flow equations.

ACKNOWLEDGEMENTS

We would like to acknowledge the financial support by the NSF under grant No. MSM8813844. We also acknowledge the computational support provided by the Pittsburgh Supercomputing Center through the Cray-Y/MP allocation time to our research, and the Academic and Computing Instructional Technology of the University of Delaware for the IBM 3090 computer time. We would also like to thank Prof. Gresho for bringing to our attention relevant work in the incompressible viscous flow simulations as well as the reviewers of the first version of the manuscript for many helpful suggestions. The many helpful discussions with Professor Karniadakis and the prompt advice of Professor Kevrekidis are also greatly appreciated.

REFERENCES

1. D. W. Beard, M. H. Davies and K. Walters, 'The stability of elastico-viscous flow between rotating cylinders. Part 3. Overstability in viscous and Maxwell fluids', *J. Fluid Mech.*, **24**, 321–334 (1966).

2. P. J. Northey, R. C. Armstrong and R. A. Brown, 'Finite-amplitude time-periodic states in viscoelastic Taylor–Couette flow described by the UCM model', *J. Non-Newtonian Fluid Mech.*, **42,** 117–139 (1992).
3. G. Capriz, G. Ghelardoni and G. Lombardi, 'Numerical study of the stability problem for Couette flow', *Phys Fluids*, **9,** 1934–1936 (1966).
4. K. A. Meyer, 'Time-dependent numerical study of Taylor vortex flow', *Phys. Fluids*, **10,** 1874–1879 (1967).
5. K. A. Meyer, 'Three-dimensional study of flows between concentric rotation cylinders', *Phys. Fluids Suppl*, **11, 12,** 165–170 (1969).
6. C. V. Alonso and E. O. Macagno, 'Numerical integration of the time-dependent equations of motion for Taylor vortex flow', *Comput. Fluids*, **1,** 301–316 (1973).
7. T. A. de Roquefort and G. Grillaud, 'Computation of Taylor vortex flow by a transient implicit method', *Comput. Fluids*, **6,** 259–269 (1978).
8. R. Meyer-Spasche and H. B. Keller, 'Computations of the axisymmetric flow between rotating cylinders', *J. Comput. Phys.*, **35,** 100–109 (1980).
9. R. D. Moser, P. Moin and A. Leonard, 'A spectral numerical method for the Navier–Stokes equations with applications to Taylor–Couette flow', *J. Comput. Phys.*, **52,** 524–544 (1983).
10. A. Chorin, 'Numerical solution of the Navier–Stokes equations', *Math. Comput.*, **22,** 745–762 (1968).
11. R. Temam, 'Sur l'approximation de la solution des equations de Navier–Stokes par la méthode des pas fractionnaires II', *Arch. Rat. Mech. Anal.*, **33,** 377–385 (1969).
12. P. Moin and J. Kim, 'On the numerical-solution of time-dependent viscous incompressible fluid-flows involving solid boundaries', *J. Comput. Phys.*, **35,** 381–392 (1980).
13. S. A. Orszag and L. C. Kells, 'Transition to turbulence in plane Poiseuille and plane Couette-flow', *J. Fluid Mech.*, **96,** 159–205 (1980).
14. L. Kleiser and U. Schumann, 'Spectral simulations of the laminar-turbulent transition process in plane Poiseuille flow', in R. G. Voigt, D. Gottlieb and M. Y. Hussaini (eds), *Spectral Methods for Partial Differential Equations*, SIAM, Philadelphia, 1984, pp. 141–163.
15. A. T. Patera, 'A spectral element method for fluid dynamics: laminar flow in a channel expansion,' *J. Comput. Phys.*, **54,** 468–488 (1984).
16. P. Le Quere and T. A. de Roquefort, 'Computation of natural convection in two-dimensional cavities with Chebyshev polynomials', *J. Comput. Phys.*, **57,** 210–228 (1985).
17. J. Kim and P. Moin, 'Application of a fractional-step method to incompressible Navier–Stokes equations', *J. Comput. Phys.*, **59,** 308–323 (1985).
18. L. Quartapelle and M. Napolitano, 'Integral conditions for the pressure in the computation of incompressible viscous flows', *J. Comput. Phys.*, **62,** 340–348 (1986).
19. S. A. Orszag, M. Israeli and M. O. Deville, 'Boundary conditions for incompressible flows', *J. Sci. Comput.*, **1,** 75–111 (1986).
20. P. M. Gresho and R. L. Sani, 'On pressure boundary conditions for the incompressible Navier–Stokes equations', *Int. j. numer. methods fluids*, **7,** 1111–1145 (1987).
21. S. C. R. Dennis and L. Quartapelle, 'Some uses of Green's theorem in solving the Navier–Stokes equations', *Int. j. numer. methods fluids*, **9,** 871–890 (1989).
22. A. G. Tomboulides, M. Israeli and G. E. Karniadakis, 'Efficient removal of boundary-divergence errors in time-splitting methods', *J. Sci. Comput.*, **4,** 291–308 (1989).
23. P. M. Gresho, 'On the theory of semi-implicit projection methods for viscous incompressible flow and its implementation via a finite element method that also introduces a nearly consistent mass matrix. Part 1: theory', *Int. j. numer. methods fluids*, **11,** 587–620 (1990).
24. P. M. Gresho, 'Incompressible fluid dynamics: some fundamental formulation issues', *Ann. Rev. Fluid Mech.*, **23,** 413–453 (1991).
25. P. S. Marcus, 'Simulation of Taylor–Couette flow. Part 1. Numerical methods and comparison with experiment', *J. Fluid Mech.*, **146,** 45–64 (1984).
26. P. S. Marcus, 'Simulation of Taylor–Couette flow. Part 2. Numerical results for wavy-vortex flow with one travelling wave', *J. Fluid Mech.*, **146,** 65–113 (1984).
27. B. K. Maulik, 'Numerical studies of the Oldroyd-B fluid stability and transition in planar channels', *Ph.D. Thesis*, Princeton University, 1989.
28. Z. Tadmor and C. G. Gogos', *Principles of Polymer Processing*, Wiley, New York, 1979.
29. T. N. Phillips and I. M. Soliman, 'The influence matrix technique for the numerical spectral simulation of viscous incompressible flows', *Research Report Aberna 25*, University College of Wales, 1988.
30. M. Avgousti and A. N. Beris, 'Viscoelastic Taylor–Couette flow: bifurcation analysis in the presence of symmetries', *Proc. R. Soc. Lond. A.* in press (1993).
31. G. Iooss and D. D. Joseph', *Elementary Stability and Bifurcation Theory*, 2nd ed., Springer, New York, 1988.
32. M. Golubitsky, D. G. Schaeffer and I. N. Stewart', *Singularities and Groups in Bifurcation Theory*, Springer, New York, 1988.
33. R. E. Lynch, J. R. Rice and D. H. Thomas, 'Direct solution of partial difference equations by tensor product methods', *Numer. Math.*, **6,** 185–199 (1964).
34. D. B. Haidvogel and T. Zang, 'The accurate solution of Poisson's equation by expansion in Chebyshev polynomials', *J. Comput. Phys.*, **30,** 167–180 (1979).

35. B. Liu, 'Numerical simulation of time-dependent flows', *Ph.D. Thesis*, University of Delaware, 1989.
36. H. C. Ku, T. D. Taylor and R. S. Hirsh, 'Pseudospectral methods for solution of the incompressible Navier–Stokes equations', *Comput. Fluids*, **15**, 195–214 (1987).
37. R. Temam, 'Remark on the pressure boundary condition for the projection method', *Theoret. Comput. Fluid Dynamics*, **3**, 181–184 (1991).
38. J. Shen, 'On error estimates of some higher order projections and penalty-projection methods for Navier–Stokes equations', *Numer. Math.*, **62**, 49–73 (1992).
39. A. T. Patera and S. A. Orszag, 'Finite-amplitude stability of axisymmetric pipe flow', *J. Fluid Mech.*, **112**, 467–474 (1981).
40. M. Avgousti, 'Viscoelastic flow instabilities: the Taylor–Couette problem', *Ph.D. Thesis*, University of Delaware, 1992.
41. R. Vichnevetsky and J. B. Bowles, *Fourier Analysis of Numerical Approximations of Hyperbolic Equations*, SIAM, Philadelphia, 1982.
42. A. N. Beris, R. C. Armstrong and R. A. Brown, 'Spectral/finite-element calculations of the flow of a Maxwell fluid between eccentric rotating cylinders', *J. Non-Newt. Fluid Mech.*, **22**, 129–167 (1987).
43. R. C. King, M. R. Apelian, R. C. Armstrong and R. A. Brown, 'Numerical stable finite element techniques for viscoelastic calculations in smooth and singular geometries', *J. Non-Newt. Fluid Mech.*, **29**, 147–216 (1987).
44. M. J. Crochet, A. R. Davies and K. Walters, *Numerical Simulation of Non-Newtonian Flow*, Rheology Series 1, Elsevier, Amsterdam, 1984.
45. S. Pilitsis and A. N. Beris, 'Calculation of steady-state viscoelastic flow in an undulating tube', *J. Non-Newt. Fluid Mech.*, **31**, 231–287 (1989).
46. I. G. Kevrekidis, B. Nicolaenko and J. C. Scovel, 'Back in the saddle again: a computer assisted study of the Kuramoto–Sivashinsky equation,' *SIAM J. Appl. Math.*, **50**, 760–790 (1990).
47. D. A. Kopriva, 'A practical assessment of spectral accuracy for hyperbolic problems with discontinuities', *J. Sci. Comput.*, **2**, 249–262 (1987).
48. E. M. Rønquist, 'Optimal spectral element methods for the unsteady three dimensional incompressible Navier–Stokes equations', *Ph.D. Thesis* MIT, 1988.